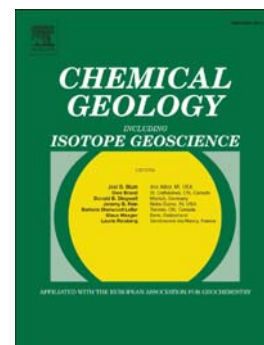Accepted Manuscript

Assessment of crystallographic orientation effects on secondary ion mass spectrometry (SIMS) analysis of cassiterite

Patrick A. Carr, Marc D. Norman, Vickie C. Bennett

Assessment of crystallographic orientation effects on secondary ion mass spectrometry (SIMS) analysis of cassiterite

Patrick A. Carr[*], Marc D. Norman and Vickie C. Bennett,

Research School of Earth Sciences, The Australian National University

Canberra, ACT 2601, Australia

*Corresponding author, email: Patrick.carr@anu.edu.au

Abstract

Crystallographic orientation effects on ion microprobe analyses for U-Pb and O-isotopes have been reported for a number of oxide minerals, including rutile (TiO_2) and baddeleyite (ZrO_2). Here we evaluate the effects of crystal orientation on U-Pb and O-isotopic data measured by ion microprobe on cassiterite (SnO_2), which is isostructural with rutile. The crystallographic orientations of mounted and polished grains of cassiterite were determined by electron backscatter diffraction (EBSD). Those grains were then analysed for U-Th-Pb isotopes and $^{18}O/^{16}O$ compositions using the SHRIMP RG and SHRIMP SI ion microprobes, respectively. Based on these data, cassiterite appears to show no dependence of key measurement parameters such as UO_2/UO, Pb/UO, or $^{18}O/^{16}O$ ratios at the achieved precision with crystallographic orientation. The contrasting behaviour of isostructural cassiterite and rutile provides new insights into the mechanisms leading to crystallographic orientation effects during ion microprobe analyses with electronic structure proposed as being a significant factor.

Keywords: Cassiterite, SIMS, crystallographic orientation effects, U-Pb, $\delta^{18}O$

Highlights:

- SIMS U-Pb and $\delta^{18}O$ isotopic compositions of cassiterite are reported for the first time.
- Unlike the isostructural rutile, crystallographic orientation of cassiterite does not appear to effect key measurement parameters.
- Electronic structure of minerals is proposed as an important feature relating to crystallographic orientation effects.

1. INTRODUCTION

Cassiterite (SnO_2), the primary ore mineral for Sn, commonly crystallises in magmatic and magmatic-hydrothermal environments associated with highly fractionated granites (e.g. Taylor 1979; Linnen 1998; Blevin 2004). Cassiterite is resistant to chemical and physical abrasion and can survive hydrothermal overprinting events and often concentrates in detrital deposits. The geochemical characteristics of cassiterite are being used increasingly to study the processes and conditions that create tin mineralisation and related ore deposits including using the oxygen isotopic compositions of cassiterite and coexisting phases for thermometry (Macy and Harris, 2006) and tracing the source of mineralising fluids (Sun and Eadington 1987; Plimer 1991; Haapala 1997; Jiang et al. 2004; Abdalla et al., 2008). In addition, trace element concentrations within cassiterite have been used for source tracing (e.g. Plimer 1991; Jiang 2004), Those studies have shown that cassiterite often incorporates moderate amounts of U and tends to exclude initial Pb (Zagruzina et al. 1987), which makes it amenable to dating using U-Pb isotopic systems (Gulson and Jones, 1992; Liu et al., 2007 Yuan et al., 2008, 2011; Li et al., 2016).

Although many cassiterites have relatively simple, monogenetic growth textures, others have more complex textures that might indicate later episodes of alteration or recrystallization that could compromise or obscure analyses of bulk samples (Fig.1). This has motivated the application of *in-situ* analytical techniques such as ion microprobe and laser ablation ICPMS for U-Pb dating (Yuan et al., 2011; Chen et al., 2014; Zhang et al. 2015; Li et al. 2016) and ion microprobe oxygen isotopic analysis of cassiterite as the high spatial resolution provided by these techniques allows specific textural zones to be targeted for analysis. In addition, cassiterite is a common accessory mineral in a variety of metal deposits including Nb-Ta (e.g. Sweetapple et al. 2002), Au (e.g. Thompson et al. 1999) and Cu-Pb-Zn (Audétat et al. 2000a,b) so that techniques requiring small amounts of material are advantageous.

A number of previous studies have applied in-situ laser ablation ICPMS analyses for U-Pb dating of cassiterite (e.g., Liu et al., 2007. Yuan et al., 2008, 2011; Blevin and Norman, 2010; Li et al., 2015; Cao et al., 2016) but to our knowledge, no U-Pb or O-

isotope studies of cassiterite by secondary ionisation mass spectrometry (SIMS) have been reported. Caution is warranted, however, because previous studies have demonstrated large crystallographic orientation effects on SIMS analyses of rutile (Li et al. 2010, 2011; Taylor et al. 2012; Schmitt & Zack 2012; Shulaker et al. 2015), which is isostructural with cassiterite, as well as for other simple structured oxides and sulphides including baddeleyite (Wingate & Compston, 2000; Li et al. 2010; Schmitt et al. 2010), magnetite (Lyon et al. 1998; Huberty et al. 2010; Kita et al. 2011), sphalerite and galena (Kozdon et. al. 2010).

Although crystallographic orientation effects during SIMS analysis of some materials have been well-documented, the physical processes that produce the effects are poorly understood (Lyon et al. 1998; Wingate & Compston, 2000; Huberty et al. 2010; Kozdon et. al. 2010; Li et al. 2010, 2011; Schmitt et al. 2010; Kita et al. 2011; Taylor et al. 2012; Schmitt & Zack 2012). The crystallographic orientation of the target mineral relative to the incoming ion beam appears to exert a control over the total sputter yield, secondary ion counts and secondary ion energies. Importantly the crystallographic orientation of some minerals can affect inter-element and isotopic fractionation, and oxide production.

Previous studies demonstrated that rutile displays some of the largest effects that have been observed so far (Li et al. 2010, 2011; Taylor et al. 2012; Schmitt & Zack 2012; Shulaker et al. 2015). Taylor *et al.* (2012) showed that the crystallographic orientation of rutile affects the total signal as measured on the reference mass ($Ti_3O_3^+$), as well as the measured UO_2^+/UO^+ ratio. They also showed that inaccurate estimations of the UO_2^+/UO^+ ratio can lead to 15% error in calculated ages of unknowns. Cassiterite is isostructural with rutile, being tetragonally coordinated with a 42mnm space group, although the unit cell dimensions of the two minerals differ slightly (cassiterite: a=4.738, c= 3.118; rutile: a= 4.594, c= 2.958).

Thus knowledge of potential orientation effects is essential prior to SIMS analyses of cassiterite to determine U-Pb and O-isotopic compositions. Here we evaluate these effects using the SHRIMP RG and SHRIMP SI ion microprobes. Crystallographic orientations of the cassiterite grains and sub-grains were determined by electron backscatter diffraction (EBSD), followed by SHRIMP analyses of these grains.

2. SAMPLES

Three cassiterite samples were used in this study. Cassiterite from the Yankee lode in the New England Orogen of eastern Australia and from near Euriowie in the Curnamona Province of central Australia were analysed for U-Pb isotopes. Cassiterite from within the Elsemore Granite in the New England Orogen was analysed for O isotopes as it appears to be relatively homogenous at the scale of ~5 mg multi-grain samples as measured by fluorination techniques (2.0 ± 0.3 ‰; Norman and Blevin, unpublished data obtained from GNS Science Lower Hutt, NZ).

The Yankee cassiterite occurs in veins associated with the Mole Granite, the age(s) of which are poorly defined. Kleeman et al. (1997) reported Ar and Rb-Sr isotopic data that implied emplacement of the Mole granite at 246 ± 2 Ma with hydrothermal and geothermal activity persisting in the area for about 15 Ma. They proposed cessation of widespread hydrothermal activity (~300°C) at 243 ± 2 Ma based on a variety of fluid-related associations (see also Audétat et al. 2000a,b). Recent TIMS U-Pb dating of zircon, monazite, and xenotime associated with the Mole granite system by Schaltegger et al. (2005) documents a ~3 Ma interval between the crystallisation of magmatic zircon within the granite at 247.7 ± 0.5 Ma to late-stage hydrothermal monazite at 244.4 ± 1.4 Ma. The Elsemore cassiterite occurs within a greisen hosted by the Elsemore Granite (Brown & Stroud 1997). Like the Mole Granite, the Elsemore Granite is Middle Triassic in age but it has not been dated isotopically.

Cassiterite occurs in structurally controlled pegmatites in the Proterozoic Curnamona Province of central Australia. The age of the pegmatites and Sn mineralisation has not been measured isotopically. Anatexis prior to and during major deformation events (D_1–D_3; e.g. Fitzherbert 2015) involved extensive partial melting and efficient melt extraction (White & Powell 2002; White *et al.,* 2004) leading to granitic magmatism between 1597 and 1591 Ma (Page *et al.* 2000). Burton (2000) suggests that the pegmatites originated from late fluids derived from the undated Texas Bore Gneissic Leucogranite, which is lithologically similar to the 1591 ± 5 Ma Mundi Mundi type granites (Page et al., 2000). A minimum age constraint is provided by the Cambrian deformation associated with the Delamerian Orogeny (Burton et al. 2000).

4

3. Methods

3.1 Polishing

Whole rock samples were crushed to <420 μm, a high density (>3.3 g/cm^3) concentrate was prepared using heavy liquids, and the handpicked cassiterite grains were mounted randomly into epoxy discs. The mounts were polished with 1200 grade abrasive paper followed by a 9, 3 and 1 μm diamond polish. Although the mounts were suitable for most microbeam analytical techniques at this point, a further 30 minutes of polishing with alumina powder and approximately 2 hours with colloidal silica was needed to remove the fine scratches caused by the diamond paste as these can affect measurements of crystallographic orientations as described below. Because of the extreme difference in hardness between the cassiterite grains and epoxy resin, this process created significant surface relief, which could have affected the SIMS analyses. Thus following the grain orientation measurements by EBSD and prior to SHRIMP analysis the mount was repolished to flatness with 1 μm diamond paste.

3.2 Cathodoluminescence imaging

Internal textures within cassiterite were imaged by cathodoluminescence (CL) using a scanning electron microscope (SEM). Polished grain mounts were carbon coated and imaged using into a JEOL JSM-6610 SEM with a Robinson CL detector at the RSES, ANU with a operating voltage of 20 keV and working distance of ~20 mm.

3.3. Crystallographic orientations

Crystallographic orientations were determined for the Yankee and Elsemore grains using a Zeiss UltraPlus analytical field emission SEM with an Oxford Instruments EBSD detector at the Centre of Advanced Microscopy, ANU, using a tungsten filament with an acceleration voltage of 20 keV and spot diameter of 60 μm. Orientations were determined by spot analysis. Several grains displayed multiple crystallographic orientations which coincided with textural domains identified in CL imaging (Figure 1). Each domain was analysed at least three times and measured backscattered patterns were compared to the match unit of Bolzan et al. (1997). All solutions had mean angular deviation (MAD) values of <1. Data processing was completed using the Oxford Instruments Channel 5.10 software with the Mambo sub-program. The CL

5

images were used to ensure that the same crystallographic domains analysed by EBSD were analysed by SHRIMP.

3.4. U-Th-Pb isotopes

U-Th-Pb isotopic compositions were measured on the SHRIMP RG over two sessions at the Research School of Earth Sciences, ANU. A 10 keV primary ion beam of O_2^- was focussed to a spot ~20 μm in diameter. Primary ion currents were ~4.6 nA during the first session and ~5.9 nA during the second session. Each analysis included an initial two-minute raster over the spot area to remove surficial Pb contamination. Positive sputtered ions were extracted at 10 keV and analysed at a mass resolution of ~6,000, sufficient to resolve most potential isobars from the Pb and U species of interest (Figure 2). Lead (Pb) masses were located using a mass offset from the dominant adjacent Sn peaks. The run table used for the two sessions is detailed in Appendix 1. The molecule $^{124}Sn_2^{16}O_2^+$ (AMU = 280) was used as a reference mass for estimates of concentration. During both sessions a single grain, with a single crystallographic orientation was analysed repeatedly as an internal reference. The data were reduced using SQUID 2.5 (Ludwig 2009). Because there is no international reference material for U-Pb isotopic analysis of cassiterite, all U-Pb ages reported here were calibrated against grains of the Yankee cassiterite assuming radiogenic $^{206}Pb/^{238}U$ and $^{207}Pb/^{206}Pb$ values of 0.0384 and 0.5105, respectively, corresponding to an age of 243 Ma (Kleeman et al., 1997).

In a target with homogenous Pb/U the relative ionisation of Pb and U is proportionate to the ratio of U oxide species (typically UO_2/UO, UO/U or UO_2/U; Hinthorne et al. 1979; Compston 1984). We followed procedures used previously for rutile by comparison against UO_2^+/UO^+. A mean relative sensitivity factor (RSF) is calculated for all standard analyses using the mean UO_2^+/UO^+, corresponding to the average analytical conditions for the session, using the formula:

$$Pb^+/UO^+ = RSF_{st} \times (UO_2^+/UO^+)^E \qquad (1)$$

where E represents the slope of covariance defined by $\ln(Pb^+/UO^+)$ and $\ln(UO_2^+/UO^+)$ (Taylor *et al*, 2012; Schmitt & Zack 2012). The true Pb/U ratios of the unknown (unk) are then calculated using the individual RSF of each unknown analysis (calculated using equation 1) in the following equation:

$$(Pb/U)_{unk} = (RSF_{unk}/RSF_{st}) * (Pb/U)_{st} \tag{2}$$

where Pb/U (st) is the true or ideal value of the standard, either assumed or measured by an independent technique.

3.5. Common Pb corrections for U-Pb SHRIMP data

Direct measurement of common Pb (monitored using ^{204}Pb) of cassiterite by SIMS is difficult due to the generally low concentrations and an isobaric interference between $^{186}W^{18}O^+$ and ^{204}Pb, requiring a mass resolution of ~10 000. Similarly, there is an isobaric inference between $^{120}Sn_4^{16}O^{++}$ and $^{232}Th^{16}O^+$ (see section 4.3) that would require a mass resolution of ~12000 to separate the two peaks. However, at 12000 mass resolution only approximately 70% of secondary ions are transmitted through the source slit, compared to approximately 90% transmission at 6000 mass resolution. Achieving the resolution required to separate these species would be at the expense of net counts, which are already low, and thus not practical.

In the Yankee and Euriowie cassiterite the highest count rates are on $^{206}Pb^+$ followed by $^{207}Pb^+$ followed by $^{208}Pb^+$. To correct for common Pb in age calculations we apply both the 207-method for higher count rates and the 208-method for its reliability in low Th/U minerals (Zack et al. 2011). Thorium concentrations in cassiterite are predominantly <0.1 ppm (Gulson & Jones 1992; Jiang et al. 2004; Li et al. 2016). Corrections were applied post-analysis using age-appropriate (243 Ma and 1585 Ma respectively) common Pb compositions from the Stacey & Kramers (1975) terrestrial model: Yankee cassiterite: $^{206}Pb/^{208}Pb$ = 0.474, $^{207}Pb/^{208}Pb$ = 0.413; Euriowie cassiterite: $^{206}Pb/^{208}Pb$ = 0.449, $^{207}Pb/^{208}Pb$ = 0.431. The reference Yankee cassiterite grain contained negligible common Pb and no corrections were required.

3.6. Oxygen isotopic compositions

Oxygen isotopic compositions ($\delta^{18}O$, where $\delta^{18}O = \left(\dfrac{\left(\frac{^{18}O}{^{16}O}\right)\text{sample}}{\left(\frac{^{18}O}{^{16}O}\right)VSMOW} - 1 \right) * 1000$) of the

Elsemore cassiterite were measured during a single session using the SHRIMP SI at the Research School of Earth Sciences, ANU. A primary Cs^+ beam of 12 nA was

focussed to a ~25 µm spot. A single cassiterite crystal with one crystallographic orientation was used as a reference throughout the session, assuming a $\delta^{18}O$ value of 2.0 ± 0.3 ‰ based on bulk fluorination analysis of the Elsmore cassiterite (Section 2). Negative sputtered ions were extracted from the sample at 10 keV. The $^{16}O^-$ and $^{18}O^-$ isotopes were measured simultaneously with two Faraday cups (Ickert et al. 2008) at a mass resolution of 10000 and the data were processed using the POXI in-house software. All analyses were normalised to the composition of the single orientated reference crystal.

4. RESULTS

4.1. Cathodoluminescence Imaging

Cassiterite is opaque or translucent to reddish brown in transmitted light depending on its chemical composition. Internal textures in opaque grains are difficult to identify by light microscope techniques and so cathodoluminescence (SEM-CL) imaging was used to examine internal characteristics of individual grains. The textural features revealed by CL primarily originate from the substitution of Ti, Fe and W for Sn (e.g. Farmer et al. 1991). Titanium and W quench the afterglow and result in dark features, whilst Fe is a luminescence activator and results in light features.

Internal textures of the Yankee and Elsemore cassiterite defined by the CL imaging are illustrated in Figures 3 and 4. The Yankee cassiterite displays primary growth textures of concentric and sector zoning, with minor secondary alteration. Linear banding of light and dark zones, commonly concentric, is ubiquitous. Bands range between 1–200 µm in thickness and have both abrupt and diffuse boundaries. This banding can be both cyclic, showing repeating light to dark transitions (=Figure 3E, F and H) and gradational from light to dark (or dark to light) (=Figure 3B and D). Sector zoning is also common and always defined by dark features (Figure 3A). This does not preclude chemical zoning in non-activator elements. In some grains the boundary between sector and concentric zoning is defined by a change in crystal orientation (Figure 1) and elsewhere only by chemical composition. Mineral inclusions (mica) are common in the Elsemore cassiterite but rare in the Yankee cassiterite. Secondary features are common in both deposits and are readily identifiable by CL imaging. Generally these consist of alteration along cracks and at the boundaries that show up as extremely bright CL.

Internal textures of the Euriowie pegmatitic cassiterite grains are displayed in Figure 4. The rhythmic banding observed in the Yankee and Elsemore cassiterite is rare in the Euriowie cassiterite (Figure 4A). Instead textures are dominantly defined by curved, discontinuous and diffuse bands of light and dark features creating an overall mottled appearance. Single bands rarely exceed 150 μm in length and are mostly less than 50 μm wide. Grains are commonly cracked and include numerous, strong luminescent (extremely bright) inclusions.

4.2. Crystallographic orientations

Crystallographic orientation data (Appendix 2) for the Yankee and Elsemore cassiterite grains are displayed in an inverse pole figure (Figure 5A), which shows the angular differences between the sample and a reference frame (Bolzan et al. 1997). The three reference planes displayed (001), (100) and (110) represent rotations around the a, b, and c axes. Cassiterite has two major crystal faces, (100) and (110) (Figure 5B) which are imperfect and indistinct respectively, whilst (001) is not a recognised terminal plane.

After crushing and milling, cassiterite separates generally displayed dominantly conchoidal fractured surfaces rather than the terminal growth faces shown in Figure 5B. This is evident in Figure 5A by a scattering of crystallographic orientations in both the Yankee and Elsemore cassiterite. There is a scarcity of data points from both samples near to the (001) plane. The Elsemore cassiterite shows a slight preference for surfaces towards the (100) plane compared with the Yankee cassiterite.

4.3 Pb/U data and relative sensitivity calibration for SHRIMP

Sixteen of the Yankee cassiterite grains containing 26 defined crystallographic domains were analysed by SHRIMP RG. Another 10 grains of the Euriowie cassiterite with unknown crystallographic orientations were also analysed. These data are presented in Appendix 3.

All measured Pb/U ratios were corrected by normalisation to a single reference crystal of Yankee cassiterite. This single crystal displayed a restricted range in counts per second (Cts/s) on the $^{124}Sn_2^{16}O_2^+$ reference mass (11158–13975 cts/s), UO_2^+/UO^+ (3.45–4.24) and $^{206}Pb^+/^{254}UO^+$ (0.074–0.135).

Measured $^{206}Pb^+/^{238}U^+$ values of cassiterite grains analysed as unknowns were 20–35 times higher in the Yankee cassiterite and 9–19 times larger in the Euriowie cassiterite than the ideal values calculated from the assumed ages (243 Ma and 1590 Ma respectively). Ionisation of UO_2^+, UO^+ and U^+ relative to ^{206}Pb of all crystallographic orientations displayed linear relationships in the approximate proportions 42:11:1 respectively for the Yankee cassiterite (Figure 7A) and 23:13:1 for the Euriowie cassiterite (Figure 7D).

The range in UO_2^+/UO^+ (3.20–4.39) and $^{206}Pb^+/^{254}UO^+$ (0.073–0.135) in the Yankee grains analysed as unknowns was slightly larger than the single crystal (Figure 6A) The Euriowie cassiterite varied slightly more with UO_2^+/UO^+ between 1.338 and 3.131, and $^{206}Pb^+/^{254}UO^+$ between 0.224 and 0.517. Despite this variation, there is no apparent relationship between counts on the reference peak and UO_2^+/UO^+ values for either sample (Figure 7B and D).

The covariance between Pb^+/UO^+ and UO_2^+/UO^+ in the Yankee cassiterite analyses is relatively restricted, and could be described by either a linear or a power function in order to define 'a' in Equation 1 (Figure 8). The Euriowie cassiterite displays a more extended array than the Yankee cassiterite in Figure 8. A regression through these data defines a power function with a slope of 0.780.

4.4 SHRIMP Pb/U cassiterite ages

4.4.1 Yankee cassiterite

The calculated RSF values from the Yankee cassiterite range between 0.0297 and 0.0403 compared to the calculated weighted mean RSF of the reference grain (0.0312 ± 0.001 or 3.4%). After correcting for the sputtering bias using Equations 1 and 2, $^{206}Pb/^{238}U$ values ranged between 0.03531 and 0.04795. An F-test indicates these compositions define a single population with a weighted mean of 0.03905 ± 0.00072 (1.9%), slightly higher than the assumed ideal value at 243 Ma (0.0384) and corresponding to an age of 246.9 ± 4.5 (1.8 %).

Common Pb was then corrected using the 207 and 208 methods. Cassiterite rarely contains significant amounts of ^{232}Th for 208 corrections (Gulson & Jones 1992; Jiang et al. 2004; Li et al. 2016). However, quantifying the Th concentration for the 208-method is difficult due to an isobaric interference with ^{120}Sn$_4$^{16}O^{++}. This is illustrated in Figure 9A which shows a strong correlation between the reference mass and ^{232}Th^{16}O$^+$. However if ^{208}Pb was the daughter product of ^{232}Th, and ^{232}Th was in equilibrium with ^{238}U, its concentration within cassiterite should correlate with the concentration of radiogenic ^{206}Pb. Figure 9B and C show that ^{208}Pb$^+$ and ^{206}Pb$^+$ are not correlated in both the Yankee and Euriowie cassiterite. The comparable common Pb age estimations by the 207 and 208 methods (see below) also indicate very little radiogenic ^{208}Pb in either of these cassiterite samples.

Common ^{206}Pb (using a ^{208}Pb correction) was as high as 18% in the Yankee cassiterite, but for most samples <4%. Age estimations for individual crystallographic domains are displayed in Table 1. Using the 208-correction method reduced the weighted mean ^{206}Pb/^{238}U age to 242.9 ± 4.8 (1.8%), which is identical to the current best age estimate of 243 Ma. Similarly, use of the 207-correction method reduced the weighted mean age to 243.9 ± 4.8 (1.8 %). The analysis requiring the highest (18%) common ^{206}Pb correction (Y6.1.2) had an uncorrected ^{206}Pb/^{238}U age of 302 ± 16 Ma, and 208- and 207-corrected ages of 246 ± 17 Ma and 245 ± 13 Ma respectively, indicating an appropriate initial common Pb ratio was used. Notably after all corrections there is no relationship between the crystallographic orientation of the Yankee cassiterite grains and counts on the reference mass, UO$_2$$^+$/UO$^+$ or Pb$^+$/UO$^+$ values (Figure 10) and calculated ages (Table 1).

4.4.2 Euriowie Cassiterite

The RSF for individual analyses of the Euriowie cassiterite is calculated from the mean UO$_2$/UO of the standard (Section 3.4) assuming a perfect fit of the regression, and that the UO$_2$/UO values of the standard and sample are comparable. However as the UO$_2$/UO values between the Euriowie cassiterite and the standard do not overlap (Figure 10) additional uncertainty must be included. This error was quantified using a robust regression analysis within ISOPLOT (Ludwig 1991). As shown in Figure 8, this results in Euriowie cassiterite analyses with UO$_2$/UO values more similar to that of the Yankee cassiterite having lower associated error.

11

The resulting calculated $^{206}Pb/^{238}U$ ages for the Euriowie cassiterite have large errors for individual analyses (200–300 Ma) and the error-weighted ages and are not practical for precise age dating. Using a calibration slope of 0.7799 leads to sputter-corrected, mean-weighted, and 208-corrected $^{206}Pb/^{238}U$ age of 1433 ± 100 Ma and a 207-corrected $^{206}Pb/^{238}U$ age of 1413 ± 110 Ma, both of which underestimate the 208-corrected $^{207}Pb/^{206}Pb$ age. A calibration slope of 1 still appropriately defines the array in Figure 8 and leads to 208-corrected and 207-corrected $^{206}Pb/^{238}U$ ages of 1534 ± 110 Ma and 1521 ± 120 Ma respectively. With this calibration slope, RSF values range between 0.137 and 0.184 and sputter-corrected $^{206}Pb/^{238}U$ values between 0.233 and 0.313. The mean-weighted uncorrected $^{206}Pb/^{238}U$ age was 1539 ± 110 Ma (3.0%) Ma.

Measured $^{207}Pb/^{206}Pb$ values ranged between 0.089–0.252, with a mean-weighted average of 0.1029 ± 0.0038 (3.7 %; 95% conf.), slightly higher than the ideal value (0.09819). Individual analyses often have large errors in calculated ages (>100 Ma; Table 2). The uncorrected mean-weighted $^{207}Pb/^{206}Pb$ age was 1666 ± 51 (3.0; 95% conf.) Ma. Calculated common ^{206}Pb (208) was as much as 7%, but predominantly below 2%. The mean weighted 208-corrected $^{207}Pb/^{206}Pb$ age from all analyses was 1588 ± 42 (2.6%; 95% conf.) Ma.

4.4. Oxygen isotope results

The results of SHRIMP II oxygen isotope determination of the Elsemore Cassiterite are compiled in Appendix 4. Count rates on ^{16}O from the reference grain of Elsemore cassiterite varied between 2.289 × 10^9 – 2.781 x10^9 cts/s, whilst the data for all grains varied only slightly more between 2.301 x 10^9 – 2.889 x10^9. Conventional fluorination analysis of the Elsmore cassiterite yielded a weighted mean $\delta^{18}O$ of 2.0 ± 0.3 ‰ for six splits of ~5 mg each. This value was assigned as the calibration value for the single crystal used for reference. Apparent $\delta^{18}O$ values for this reference grain ranged between 1.15 and 2.82 ‰, giving an uncertainty on the weighted mean value (1.98) of ± 0.16 ‰ (95% conf.). Apparent $\delta^{18}O$ values of the Elsemore grains analysed as unknowns varied between 1.18 and 3.43 ‰, with a weighted average of 2.22 ± 0.11 ‰ (95% conf), within error of the reference grain (Figure 11). Standard error estimates for individual analyses ranged between 0.08 and 0.65‰. Numerous measurements were taken on individual crystallographic orientation domains. These data are

summarised in Table 3. Whilst $\delta^{18}O$ values vary significantly between these domains, there is no apparent relationship between crystallographic orientation and $\delta^{18}O$ values (Figure 12). Compositions measured within a single crystallographic orientation varied by as much as 1.5‰ suggesting large internal heterogeneity. There is a grouping of 4 analysis ~15° from the 100 plane and ~80 ° from the 001 plane with a high ^{16}O count rate (Figure 12; circled). This is a similar orientation to that for maximum count rate from rutile reported by Taylor et al. (2012) in rutile (78° from 001, 15° from 110).

5. Discussion:

5.1. Crystallographic orientation effects on SIMS U-Pb data

In their SIMS analyses of rutile, Taylor *et al.* (2012) showed variable ionisation of UO^+ relative to $^{206}Pb^+$ compared with UO_2^+ relative to $^{206}Pb^+$ (Figure 7E). Similarly they documented variations of between 300–1800 total counts on the reference mass ($^{48}Ti_3^{16}O_3^+$) that co-varied with UO_2^+/UO^+ (Figure 7F), with high total counts on the reference mass being associated with high UO_2^+/UO^+. Those authors proposed primary ion channelling – the implantation of primary ions along particular crystallographic planes - resulted in variable sputtering rates. Orientations with higher sputter rates (shallower ion implantation) consumed more O at the interface of the primary beam and sample surface than low sputtering rates (deeper ion implantation; Schmitt & Zack, 2012). Increased consumption of this O lead to the variable ionisation of UO^+ relative to UO_2^+ that affected sputtering calibrations relying on this ratio (Equation 1).

It is difficult to identify such effects in our data despite large variations in cts/s on the $Sn_2O_2^+$ reference mass (10327–19078 cts/s). Within the single orientation domain on the reference grain (Y12), cts/s on the reference mass varied between 11158 and 13975. If ion channelling is occurring it appears to be insignificant relative to variations in primary beam intensity or ion yields. Measured UO_2^+/UO^+ values in the Yankee (3.20–4.39) and Euriowie cassiterite (1.34–3.13) varied slightly more than observed by Taylor et al. (2012) for rutile (0.57–1.48). However the percentage variation of UO_2^+/UO^+ in rutile is more than double that of the Yankee cassiterite. Unlike rutile there is no covariance between total counts on the reference mass and UO_2^+/UO^+ in the Yankee (Figure 7B) and Euriowie cassiterite (Figure 7D) and most importantly the

variable ionisation of UO^+ in rutile reported by Taylor et al. (2012) (Figure 7E) is clearly not present in cassiterite (Figure 7A and C).

Calculated $^{206}Pb/^{238}U$ age estimates of the Yankee cassiterite with 26 different crystallographic orientations yielded a weighted mean error of ~5 % (Table 1). In contrast, Taylor et al. (2012) highlighted potential weighted mean errors of up to 15% were possible in rutile owing to the poorly defined calibration slope. This large error is attributed to the large variation in UO_2^+/UO^+ values associated with crystallographic orientation.

5.2. $\delta^{18}O$ variations in the Elsemore cassiterite: real or analytical uncertainty?

Cassiterite commonly forms in complex geological environments with dramatically changing temperatures and numerous fluid sources (e.g. Sun and Eadington 1987; Ren et al., 1995) and thus the $\delta^{18}O$ values within cassiterite can be expected to vary. The two methods providing the most precise $\delta^{18}O$ determinations in a wide range of samples are fluorination, by which bulk samples (> 5 mg) are reacted with F_2 or BrF_5 to create O_2, and laser fluorination, which rapidly and efficiently heats the sample to produce O_2 and requiring > 0.3 mg of bulk separates. However in both these bulk techniques, inter- and intra-grain heterogeneities cannot be assessed. Cassiterite geothermometry by these methods, which is based on the temperature dependent fractionation of oxygen isotopes between quartz and cassiterite (e.g. Hu et al. 2005), assumes that all grains analysed are in isotopic equilibrium and are internally homogeneous.

The SHRIMP SI results reported here indicate that the $\delta^{18}O$ measured on a cassiterite crystal with a single crystallographic orientation can vary by as much as ~2‰. During SIMS analysis of oxygen isotopes the dominant source of instrumental mass fractionation is the composition of the target mineral. Therefore the ~2‰ variation observed in a single homogenous composition cassiterite grain is likely an approximation of the true internal O isotopic heterogeneity in that grain. Determining whether variations outside this range are real or related to differences in the crystallographic orientation is difficult. Huberty et al. (2010) reported crystallographic orientation effects in SIMS analysis of magnetite of $\delta^{18}O$ of 2–3 ‰, however within a single grain orientation the precision was 0.4 ‰ (2SD), which is more typical for O-isotopic analysis of homogeneous materials by SIMS (e.g. Ickert *et al.* 2008; Huberty

et al. 2010). At the present, it is therefore difficult to differentiate true compositionl heterogeneity from crystallographic orientation effects in the Elsemore cassiterite at a precision less than 2‰. Future work needs to identify suitably homogenous natural reference materials or develop methods to synthesize cassiterite crystals, which has proven particularly challenging (e.g. Shimada et al., 1982).

5.3. Causes of crystallographic orientation effects: cassiterite vs. rutile

The documented occurrence of large crystallographic orientation effects in rutile (Li et al. 2010, 2011; Taylor et al. 2012; Schmitt & Zack 2012; Shulaker et al. 2015) but not the isostructural cassiterite (this study) indicates that a fundamental difference unrelated to crystallographic structural parameters may contribute to crystallographic orientation effects, During SIMS analyses, the interaction between an incoming ion and a target sample is highly complex, involving numerous variables including the type of primary ion, impact angle and energy, and the composition, bond strength and structure of the sample matrix. Many models for the origin of orientation effects focus predominantly on the crystallographic structure of the target minerals (Huberty et al. 2010; Taylor et al. 2012; Schmitt & Zack 2012). This is particularly warranted for rutile and cassiterite as Lumpkin *et al.* (2010) show that both minerals maintain their crystal structure and are not amorphised under ion bombardment more intense than that experienced in SIMS. Below we briefly discuss the possible mechanisms that might contribute to crystallographic orientation effects in relation to key structural and mineral physics parameters that differ between cassiterite and rutile.

Primary ion channelling is a well-documented process, describing the implantation of primary ions along particular crystallographic planes. Primary ions entering the target mineral directed parallel to a crystallographic plane will travel deeper into the structure, whilst primary ions directed perpendicular to a crystallographic plane will interact with the top layers. Ions implanted deep into the target surface result in much less sputtered material (Benninghoven 1994). Secondary ion focussing occurs when collisional cascades are focussed along or between crystals planes, imposing a preferred orientation on secondary ions ejected from the sample (e.g. Huberty et al. 2010). There is, however, no unifying model for crystallographic orientation effects, with primary ion channelling the preferred mechanism in U-Pb studies (Schmitt & Zack

2012; Taylor et al. 2012) and secondary ion focussing in light stable isotopic studies (Huberty et al. 2010), despite a comparable relative mass difference (e.g. ^{18}O is 12.5% heavier than ^{16}O and ^{238}U is 15.5 % heavier than ^{206}Pb).

Taylor et al. (2012) showed that much of the variation in SIMS U-Pb analysis of rutile occurs over a ~5° rotation between the 010 and 110 cleavage planes. As in cassiterite (Figure 6B), these planes are parallel to the major axis of the crystal and if exposed after crushing and/or milling provide an ideal surface for mounting. Crystallographic orientation effects may therefore be exaggerated in rutile due to a preference to mount in these orientations. Conversely cassiterite in this study showed a wide variety of orientations consistent with the dominant conchoidal fracture noted in the separates. As we show here the sputtering calibration equations adequately account for much of the variation seen in UO_2^+/UO^+, resulting in accurate and moderately precise Pb/U values. We thus conclude that cassiterite does not display the predominant crystallographic orientation effect documented in rutile and suggest that for cassiterite there is a compositional control on the calculated Pb/U.

How primary ion channelling leads to variations in calculated Pb/U values is unclear. Several authors have mitigated some of the effects of crystallographic orientation during U-Pb analysis by flooding the chamber with oxygen (Schuhmacher et al. 1994; Li et al. 2010; Schmitt et al. 2010; Schmitt & Zack 2012) with the added advantage of increasing $^{206}Pb^+$ yields. In both rutile and baddeleyite this had the effect of reducing the range of UO_2^+/U^+ values and total sputter yield (Schmitt et al. 2010; Schmitt & Zack 2012). Schmitt & Zack (2012) suggested that increased sputter rates, associated with less primary ion channelling, progressively deplete the surface layer of oxygen, resulting in a larger range in UO_x^+/U^+ values. This is in agreement with Magee et al. (2014) who showed that approximately half of the O in the secondary ion beam is sourced from the sample itself, whilst the rest comes from the primary ions or gas in the vacuum chamber. Thus the availability of introduced O can affect the production of UO_x^+.

A potential contributor to the effects of crystallographic orientation effects is the large and highly variable dielectric constant of rutile (86–170) which is related to crystallographic orientation (Diebold 2003). Conversely the dielectric constant for cassiterite is low and restricted to between 9–14 (Shannon 1993). This contrast is

thought to be related to the different cell dimensions and electronic structures of the Sn and Ti oxide matrices (e.g. Kumar et al. 2011; Machesky et al. 2011; Gao et al. 2014). The strong and highly variable dielectric constant of rutile may locally alter the electronic field gradient, leading to a defocused or misaligned secondary beam dependent on the crystallographic orientation. Thus secondary beam optimisation should be undertaken to account for this variation by optimisation on numerous grains as suggested by Taylor et al. (2012). The variable ionisation of UO^+ relative to the reference mass and $^{206}Pb^+$ reported by Taylor et al. (2012) may thus be related to the variable secondary ion energy distribution of UO^+ relative to UO_2^+.

6. CONCLUSIONS

Crystallographically oriented grains of cassiterite were measured for U-Pb and O isotopic compositions by SHRIMP ion microprobes to assess the possible effects of orientation on U-Pb and oxygen isotopic measurements. The results indicate minimal, if any, effects of crystallographic orientation for cassiterite during SIMS analysis, in contrast to previous studies of the isostructural mineral rutile. Specifically, unlike rutile, the range in measured UO_2^+/UO^+ ratios and in reference mass cts/s is not sensitive to crystallographic orientation. Relatively large variations in apparent $\delta^{18}O$ within individual grains of the Elsemore cassiterite analysed here highlight the need for in-situ techniques, particularly for thermometry. In this study, the inferred intra-crystal heterogeneity of the cassiterite limits the identification of crystallographic orientation effects to <~2 ‰. The physical processes leading to these crystallographic orientation effects are still unknown, although fundamental differences in the electronic structure of cassiterite compared to rutile may be influential.

Acknowledgements

References:

Audétat, A., Gnther, D., Heinrich, C.A., 2000a. Magmatic-hydrothermal evolution in a fractionating granite: a microchemical study of the Sn-W-F-mineralized Mole granite (Australia). Geochimica et Cosmochimica Acta, 64(19): 3373-3393.

Audétat, A., Günther, D., Heinrich, C.A., 2000b. Causes for Large-Scale Metal Zonation around Mineralized Plutons: Fluid Inclusion LA-ICP-MS Evidence from the Mole Granite, Australia. Economic Geology, 95(8): 1563-1581.

Benninghoven, A., 1994. Chemical analysis of inorganic and organic surfaces and thin films by static Time-Of-Flight Secondary Ion Mass Spectrometry (TOF-SIMS). Angewandte Chemie (International Edition in English), 33(10): 1023-1043.

Blevin, P.L., Norman, M., 2010. Cassiterite; the zircon of mineral systems? A scoping study. Abstracts, Geological Society of Australia, 98: 399-400.

Bolzan, A.A., Fong, C., Kennedy, B.J., Howard, C.J., 1997. Structural Studies of Rutile-Type Metal Dioxides. Acta Crystallographica Section B, 53(3): 373-380

Brown, R.E., Stroud W.J., 1997. Inverell 1:250 000 metallogenic map SH/56-5: metallogenic study and mineral deposit data sheets, Geological Survey of New South Wales, Sydney.

Burton, G.R., 2000. Metallogenic studies of the Broken Hill and Euriowie Blocks, New South Wales. 4. Mineral deposits of the Euriowie Block (including the northernmost Broken Hill Block and Poolamacca Inlier, Bulletin 32(4). Geological survey of New South Wales.

Cao, H.-W., Zhang, Y.-H., Pei, Q.-M., Zhang, R.-Q., Tang, L., Lin, B., Cai, G.-J., 2016. U–Pb dating of zircon and cassiterite from the Early Cretaceous Jiaojiguan iron-tin polymetallic deposit, implications for magmatism and metallogeny of the Tengchong area, western Yunnan, China. International Geology Review, 59(2):234-258.

Chen, X-C., Hu, R-Z., Bi, X-W., Li, H-M., Lan, J-B., Zhao, C-H., Zhu, J-J., 2014. Cassiterite LA-MC-ICP-MS U/Pb and muscovite 40Ar/39Ar dating of tin deposits in the Tengchong-Lianghe tin district, NW Yunnan, China. Mineralium Deposita, 49(7):843-860.

Diebold, U., 2003. The surface science of titanium dioxide. Surface Science Reports, 48(5–8): 53-229.

Farmer, C.C., Searl, A., Halls, C., 1991. Cathodoluminescence and Growth of Cassiterite in the Composite Lodes at South Crofty Mine, Cornwall, England. Mineralogical Magazine, 55(380):447-458.

Fitzherbert, J., 2015. Refined peak and retrograde metamorphic isograds for the Broken Hill and Euriowie blocks, NSW. Geological Survey of New South Wales, Quarterly Notes 143(1), 1–43

Gulson, B.L., Jones, M.T., 1992. Cassiterite: Potential for direct dating of mineral deposits and a precise age for the Bushveld Complex granites. Geology, 20(4): 355-358.

Haapala, I., 1997. Magmatic and Postmagmatic Processes in Tin-mineralized Granites: Topaz-bearing Leucogranite in the Eurajoki Rapakivi Granite Stock, Finland. Journal of Petrology, 38(12):1645-1659.

Hinthorne, J.R., Andersen, C.A., Conrad, R.L., Lovering, J.F., 1979. Single-grain 207Pb/206Pb and U/Pb age determinations with a 10-μm spatial resolution using the ion microprobe mass analyzer (IMMA). Chemical Geology, 25(4):271-303.

Hu, G., Clayton, R.N., Polyakov, V.B., Mineev, S.D., 2005. Oxygen isotope fractionation factors involving cassiterite (SnO_2): II. determination by direct isotope exchange between cassiterite and calcite. Geochimica et Cosmochimica Acta, 69(5):1301-1305.

Huberty, J.M., Kita, N.T., Kozdon, R., Heck, P.R., Fournelle, J.H., Spicuzza, M.J., Xu, H., Valley, J.W., 2010. Crystal orientation effects in δ18O for magnetite and hematite by SIMS. Chemical Geology, 276(3–4): 269-283.

Jiang, S-Y.,Yu, J-M., Lu, J-J., 2004. Trace and rare-earth element geochemistry in tourmaline and cassiterite from the Yunlong tin deposit, Yunnan, China: implication for migmatitic–hydrothermal fluid evolution and ore genesis. Chemical Geology, 209(3-4):193-213.

Ickert, R.B., Hiess, J., Williams, I.S., Holden, P., Ireland, T.R., Lanc, P., Schram, N., Foster, J.J., Clement, S.W., 2008. Determining high precision, in situ, oxygen isotope ratios with a SHRIMP II: Analyses of MPI-DING silicate-glass reference materials and zircon from contrasting granites. Chemical Geology, 257(1–2): 114-128.

Kita, N.T., Huberty, J.M., Kozdon, R., Beard, B.L., Valley, J.W., 2011. High-precision SIMS oxygen, sulfur and iron stable isotope analyses of geological materials: accuracy, surface topography and crystal orientation. Surface and Interface Analysis, 43(1-2): 427-431.

Kleeman, J.D., Plimer, I.R., Lu, J., Foster, D.A., Davidson, R., 1997. Timing of thermal and mineralisation events associated with the Mole Granite. In: Ashley, P., Flood, P.G. (Editors), Tectonics and Metallogenesis of the New England Orogen, Special Publication 19. Geological Society of Australia, pp. 254-265.

Kozdon, R., Kita, N.T., Huberty, J.M., Fournelle, J.H., Johnson, C.A., Valley, J.W., 2010. In situ sulfur isotope analysis of sulfide minerals by SIMS: Precision and accuracy, with application to thermometry of ~3.5Ga Pilbara cherts. Chemical Geology, 275(3-4): 243-253.

Kumar, N., Kent, P.R.C., Bandura, A.V., Kubicki, J.D., Wesolowski, D.J., Cole, D.R., Sofo, J.O., 2011. Faster proton transfer dynamics of water on SnO2 compared to TiO2. The Journal of Chemical Physics, 134(4): 044706.

Li, Q.-L., Li, X-H., Liu, Y., Wu, F-Y., Yang, J-H., Mitchell, R.H., 2010. Precise U–Pb and Th–Pb age determination of kimberlitic perovskites by secondary ion mass spectrometry. Chemical Geology, 269(3–4): 396-405.

Li, Q.-l., Lin, W., Su, W., Li, X-H., Shi, Y-H., Liu, Y., Tang, G-Q., 2011. SIMS U–Pb rutile age of low-temperature eclogites from southwestern Chinese Tianshan, NW China. Lithos, 122(1–2): 76-86.

Li, C.Y., Zhang, R.Q., Ding, X., Ling, M.X., Fan, W.M., Sun, W.D., 2016. Dating cassiterite using laser ablation ICP-MS. Ore Geology Reviews, 72(P1):313-322.

Liu, Y., Li, Z.-X., Li, H.-M., Guo, L.-G., Xu, W., Ye, L., Li, C.-Y., Pi, D.-H., 2007. U-Pb geochronology of cassiterite and zircon from the Dulong Sn-Zn deposit: Evidence for

Cretaceous large-scale granitic magmatism and mineralization events in southeastern Yunnan province, China. Acta Petrologica Sinica. 23 (5): pp. 967-976.

Ludwig, K.R., 1991. ISOPLOT; a plotting and regression program for radiogenic-isotope data; version 2.53. USGS Open-File report, 91-445.

Ludwig, K.R., 2009. Squid 2: A User's Manual, Berkeley Geochronology Centre.

Lyon, I.C., Saxton, J.M., Cornah, S.J., 1998. Isotopic fractionation during secondary ionisation mass spectrometry: Crystallographic orientation effects in magnetite. International Journal of Mass Spectrometry and Ion Processes, 172(1-2): 115-122.

Magee, C., Ferris, J., Magee, C., 2014. Effect of impact energy on SIMS U–Pb zircon geochronology. Surface and Interface Analysis: n/a-n/a.

Page, R.W., Stevens, B.P.J., Gibson, G.M., Conor, C.H.H., 2000. Geochronology of WIllyama Supergroup rocks between Olary and Broken Hill, and comparison to northern Australia.

Paton, C., Hellstrom, J., Paul, B., Woodhead, J., Hergt, J., 2011. Iolite: Freeware for the visualisation and processing of mass spectrometric data. Journal of Analytical Atomic Spectrometry, 26(12): 2508-2518.

Plimer, I.R., Lu, J., Kleeman, J.D., 1991. Trace and rare earth elements in cassiterite – sources of components for the tin deposits of the Mole Granite, Australia. Mineralium Deposita, 26(4):267-274.

Ren, S.K., Walshe, J.L., Paterson, R.G., Both, R.A., Andrew, A., 1995. Magmatic and hydrothermal history of the porphyry-style deposits of the Ardlethan tin field, New South Wales, Australia. Economic Geology, 90(6):1620-1645.

Schaltegger, U., Pettke, T., Audétat, A., Reusser, E., Heinrich, C.A., 2005. Magmatic-to-hydrothermal crystallization in the W–Sn mineralized Mole Granite (NSW, Australia): Part I: Crystallization of zircon and REE-phosphates over three million years—a geochemical and U–Pb geochronological study. Chemical Geology, 220(3–4): 215-235.

Shulaker, D.Z., Schmitt, A.K., Zack, T., Bindeman, I., 2015. In-situ oxygen isotope and trace element geothermometry of rutilated quartz from Alpine fissures. American Mineralogist, 100(4): 915-925.

Schmitt, A.K., Chamberlain, K.R., Swapp, S.M., Harrison, T.M., 2010. In situ U-Pb dating of micro-baddeleyite by secondary ion mass spectrometry. Chemical Geology, 269(3-4): 386-395.

Schmitt, A.K., Zack, T., 2012. High-sensitivity U–Pb rutile dating by secondary ion mass spectrometry (SIMS) with an O2+ primary beam. Chemical Geology, 332–333(0): 65-73.

Schuhmacher, M., De Chambrost, E., McKeegan, K.D., Harrison, T.M., Migeon, H., 1994. In-situ dating of zircon with the CAMECA IMS 1270. In: Benninghoven, A., Werner, H.W., Shimizu, R., Nihei, Y. (Eds.), Secondary ion mass spectrometry (SIMS IX). John Wiley & Sons, pp. 919-922.

Shannon, R.D., 1993. Dielectric polarizabilities of ions in oxides and fluorides. Journal of Applied Physics, 73(1): 348-366.

Sun, S.S., Eadington, P.J., 1987. Oxygen isotope evidence for the mixing of magmatic and meteoric waters during tin mineralization in the Mole Granite, New South Wales, Australia. Economic Geology, 82(1):43-52.

Sweetapple, M.T., Collins, P.L.F., 2002. Genetic Framework for the Classification and Distribution of Archean Rare Metal Pegmatites in the North Pilbara Craton, Western Australia. Economic Geology, 97(4):873-895.

Taylor, R., Clark, C., Reddy, S.M., 2012. The effect of grain orientation on secondary ion mass spectrometry (SIMS) analysis of rutile. Chemical Geology, 300–301(0): 81-87.

Thompson, J.F.H., Sillitoe, R.H., Baker, T., Lang, J.R., Mortensen, J.K., 1999. Intrusion-related gold deposits associated with tungsten-tin provinces. Mineralium Deposita, 34(4):323-334.

White, R.W., Powell, R., 2002. Melt loss and the preservation of granulite facies mineral assemblages. Journal of Metamorphic Geology, 20:621-632.

White, A.J.R., Chappell, B.W., 2004. Petrographic Discrimination of Low- and High-Temperature I-type Granites. Resource Geology, 54(3):215-226.

Wingate, M.T.D., Compston, W., 2000. Crystal orientation effects during ion microprobe U–Pb analysis of baddeleyite. Chemical Geology, 168(1–2): 75-97.

Yuan, S., Peng, J., Hu, R., Li, H., Shen, N., Zhang, D.,2008. A precise U–Pb age on cassiterite from the Xianghualing tin-polymetallic deposit (Hunan, South China). Mineralium Deposita, 43(4): 375-382.

Yuan, S., Peng, J., Hao, S., Li, H., Geng, J., Zhang, D., 2011. In situ LA-MC-ICP-MS and ID-TIMS U–Pb geochronology of cassiterite in the giant Furong tin deposit, Hunan Province, South China: New constraints on the timing of tin–polymetallic mineralization. Ore Geology Reviews, 43(1): 235-242.

Zagruzina, I., Pinskii, E., Savinova, I., 1987. Uranium in cassiterite of tin deposits. International Geology Review, 29:94-109.

Zhang, R-Q., Lu, J-J., Wang, R-C., Yang, P., Zhu, J-C., Yao, Y., Gao, J-F., Li, C., Lei, Z-H., Zhang, W-L., Guo, W-M., 2015. Constraints of in situ zircon and cassiterite U–Pb, molybdenite Re–Os and muscovite 40Ar–39Ar ages on multiple generations of granitic magmatism and related W–Sn mineralization in the Wangxianling area, Nanling Range, South China. Ore Geology Reviews, 65(4):1021-1042.

Figures

Figure 1: Scanning Electron Microprobe (SEM) cathodoluminescence (CL) image of a Yankee cassiterite grain used in this study. The crystallographic orientation of the sectors within the grain are represented by the colour coded unit cells and major axes (red = c, green = a, blue = b). It is common in the Yankee and Elsemore cassiterite for the CL zoning to be coincident with changing crystallographic orientation.

Figure 2: SHRIMP RG mass spectra of a W-rich Yankee cassiterite grain showing A) the potential major mass interferences with ^{204}Pb) the clearly resolved ^{206}Pb peak and small to non-existent ^{207}Pb and ^{208}Pb peaks, and C) the increasing signal of U species from ^{238}U to ^{238}U^{16}O and ^{238}U^{16}O$_2$. Ionised Sn molecules are present adjacent to all peaks and can be used to specifiy the positions of small U and Pb signals with a trim offset.

Figure 3: SEM CL images of the Yankee cassiterite (A–D) and the Elsemore cassiterite (E–H) grains used in this study. White scale bars are 200 μm. The Yankee cassiterite commonly shows concentric zoning (B, C and D) and minor sector zoning (A and C). Secondary alterations and inclusions are rare but identified by bright CL response (e.g. A and C). The Elsemore cassiterite typically exhibits concentric zoning (E-F) with minor alteration along internal cracks (G) and with inclusions (E,F and G) defined by bright CL response . The bright CL inclusions are Fe- or Ti- oxides.

Figure 4: SEM CL images of the Euriowie cassiterite grains used in this study. White scale bars are 200 μm. Internal textures are curved, discontinuous and diffuse bands of light and dark features creating an overall mottled appearance. Very bright oxide inclusions are common to the Euriowie Cassiterite.

Figure 5: (A) Inverse pole figure representation of all crystallographic orientations of the Yankee and Elsemore cassiterite used in this study. Cassiterite does not show a preferred orientation when mounted into epoxy; this is in contrast to isostructural rutile (e.g. Taylor et al. 2012) B: 3D model of cassiterite with terminating surfaces labelled.

Figure 6: Variation over time between UO_2/UO^+ (A), Relative Sensitivity Factor (B) and $^{206}Pb*/^{238}U$ (C) for the Yankee cassiterite. Variations of these measured ratios on the single orientated crystal internal reference (red) are comparable with those 'unknown' measurements on all crystallographic orientations (blue).

Figure 7: SHRIMP Yankee (A and B) and Euriowie cassiterite (C and D) data used in this study compared to SIMS rutile data (E and F) of Taylor *et al.* (2012). Cassiterite in this study displays linear relationships between ^{206}Pb and the measured U species (A and C) compared to rutile which show variable ionisation of UO^+ relative to ^{206}Pb. Cts/s on the reference mass in cassiterite do not correlate with UO_2/UO values (B and D), unlike in rutile (F; Taylor et al. 2012).

Figure 8: Logarithmic calibration graph of SHRIMP U-Pb data from the Yankee and Euriowie cassiterite. The tight cluster of Yankee data defines a slope of 0.697, however the more variable Euriowie cassiterite, with a slope of 0.780, is less constrained. To account for the uncertainty due to an offset in UO_2/UO values between the Yankee reference grains and the Euriowie grains a robust regression analysis is included.

Figure 9: SHRIMP U-Pb data for cassiterite. A) Cts/s on the reference peak are correlated with $^{232}Th^{16}O^+$ indicating an isobaric interference such that Th concentrations cannot be directly measured. However, the linear correlations between ^{207}Pb and ^{206}Pb but not ^{208}Pb and ^{206}Pb indicate that most ^{208}Pb originates as common Pb in the Yankee Cassiterite (B) and the Euriowie Cassiterite (C) and can be used for common Pb corrections of the ^{206}Pb.

Figure 10: Cts/s on reference peak $Sn_2O_2^+$ (A), UO_2/UO^+ (B) and Pb/UO^+ (C) values of the Yankee cassiterite relative to crystallographic orientation depicted in an inverse pole figure. The lack of any correlation between these parameters indicates minimal effect of orientation on SHRIMP measurements.

Figure 11: All $\delta^{18}O_{VSMOW}$ Elsemore cassiterite values, normalised to a singly orientated crystal, grouped by their crystallographic orientation. Intra-grain variations for a single orientation can be as large as 1.5 ‰.

Figure 12: Cts/s on ^{16}O (A) and $\delta^{18}O$ (B) for Elsemore cassiterite relative to crystallographic orientation depicted in an inverse pole figure. A grouping of 4 analyses (circled) ~15° from the 100 plane and ~80 ° from the 001 plane with high ^{16}O count rate (A) may indicate ion channelling, however it is not manifested in the U-Pb data or the $\delta^{18}O$ values.

Figure 1

Figure 2

AMU
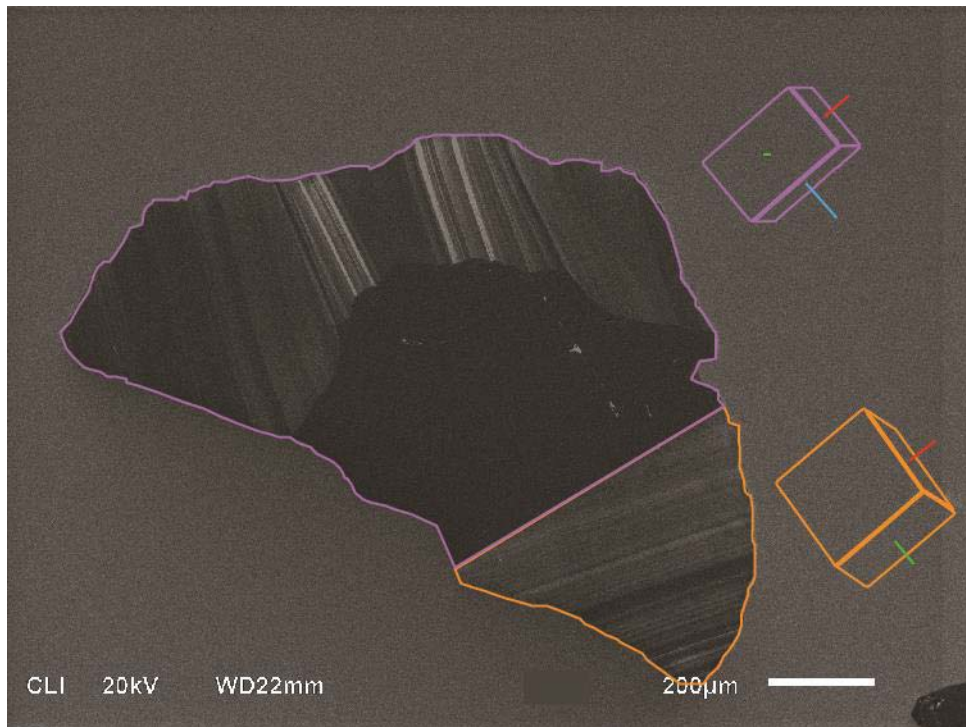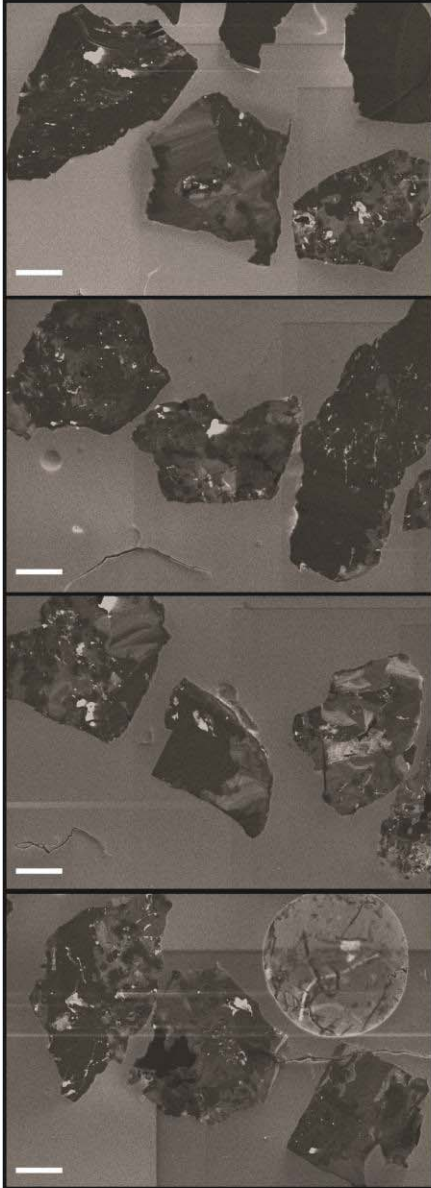
Figure 3
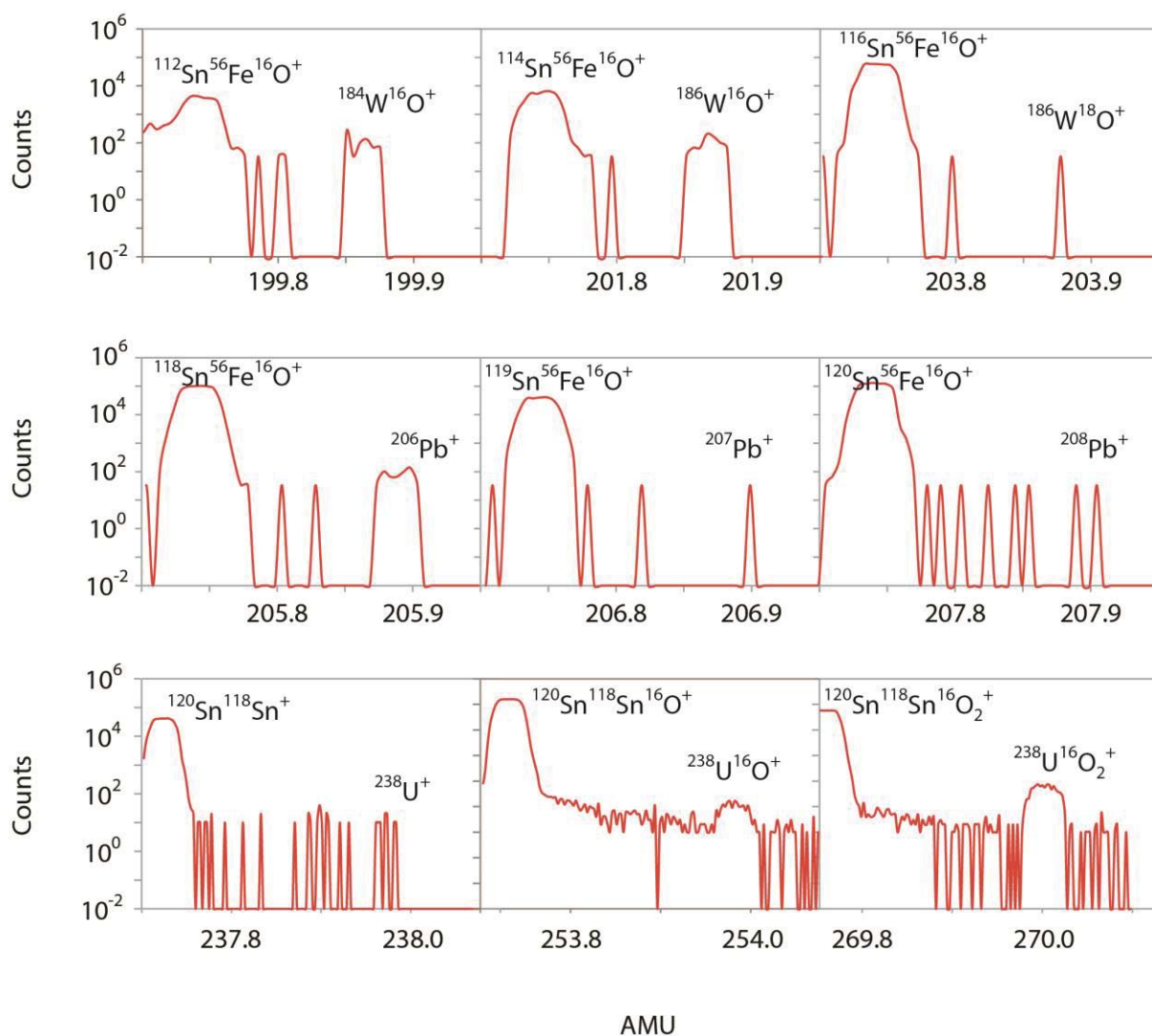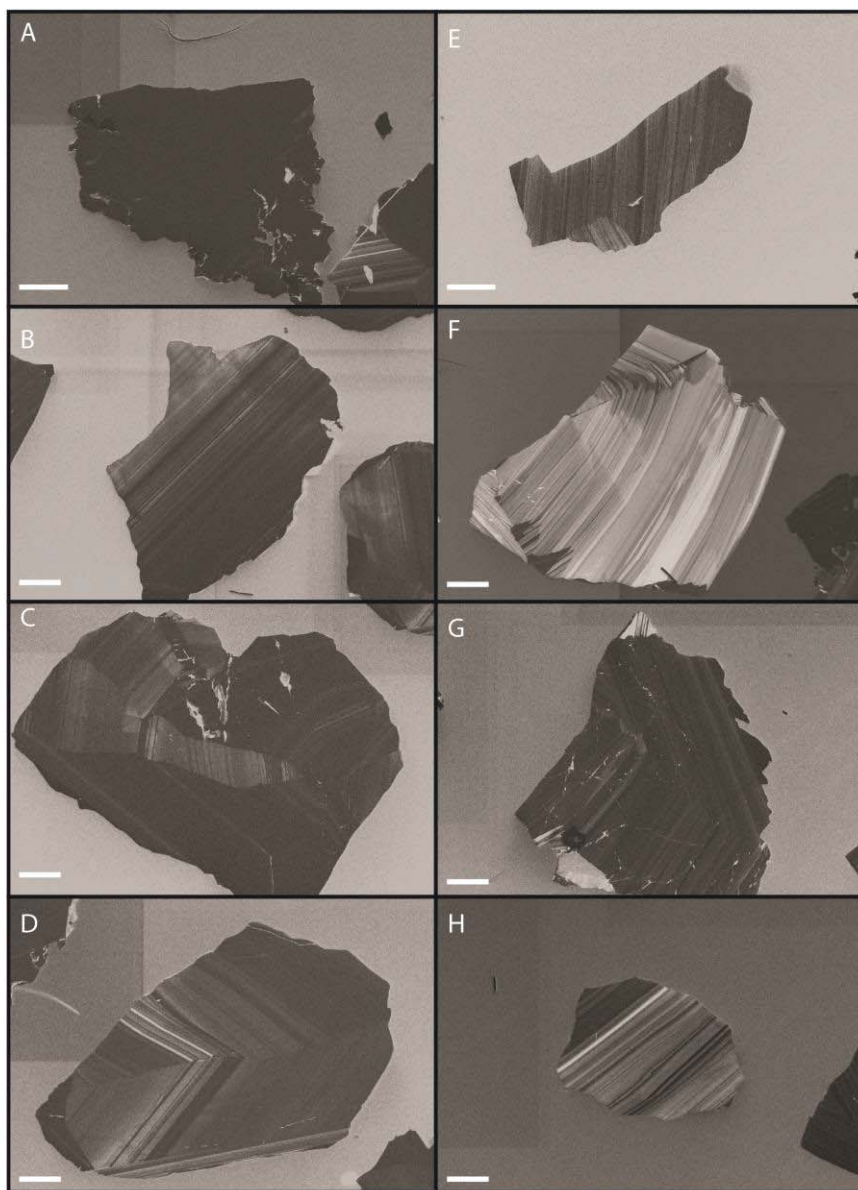
Figure 4

Figure 5
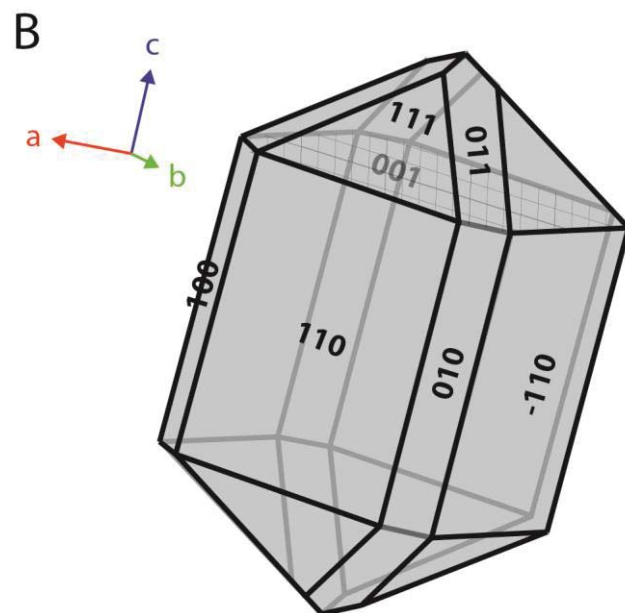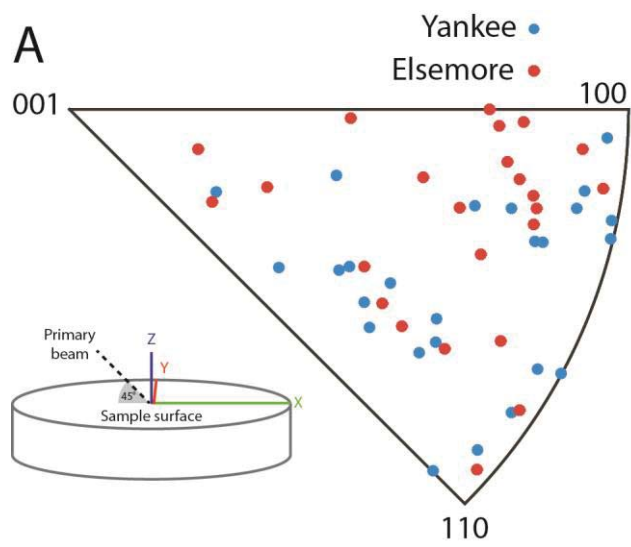
Figure 6
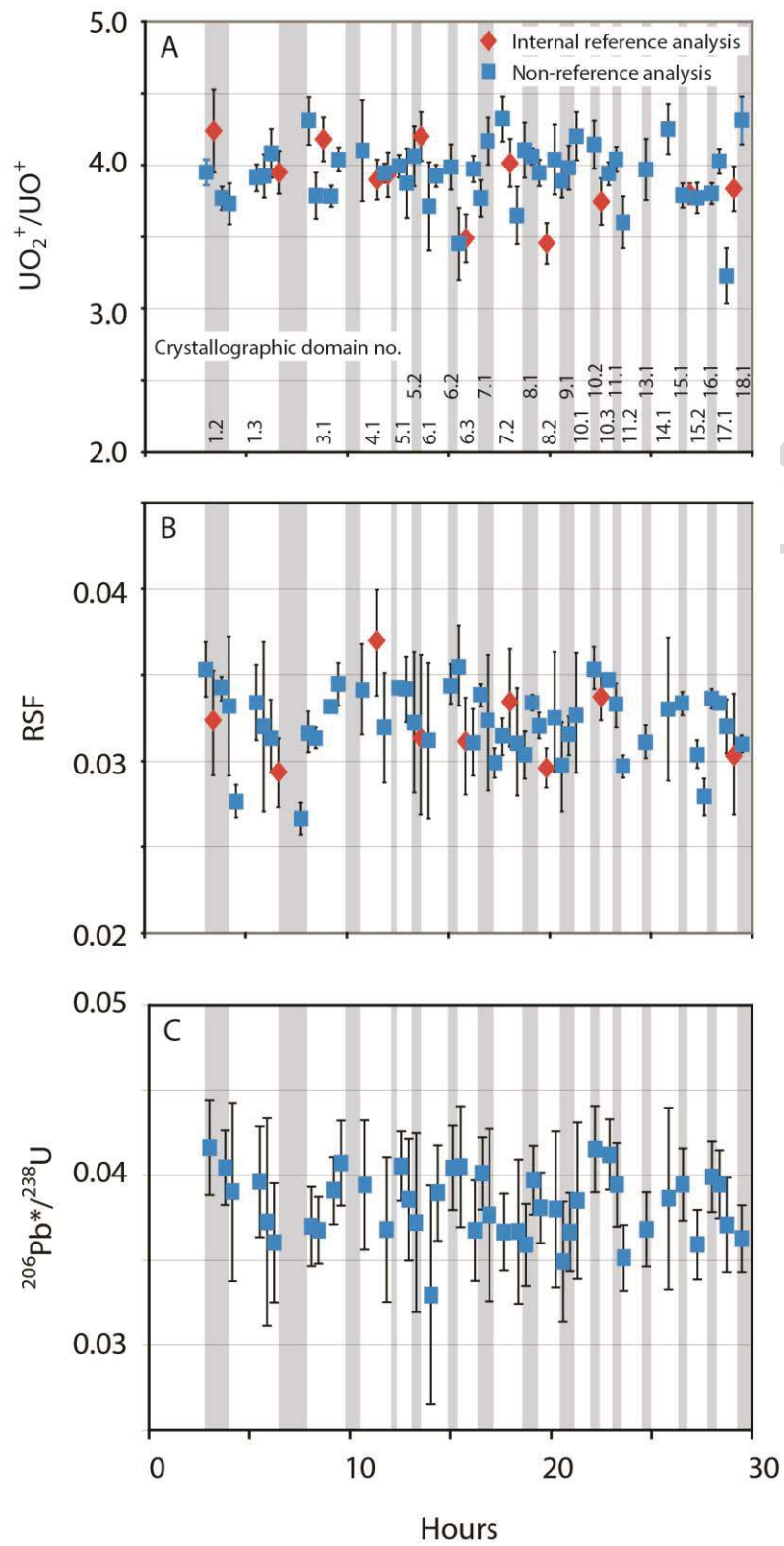
Figure 7
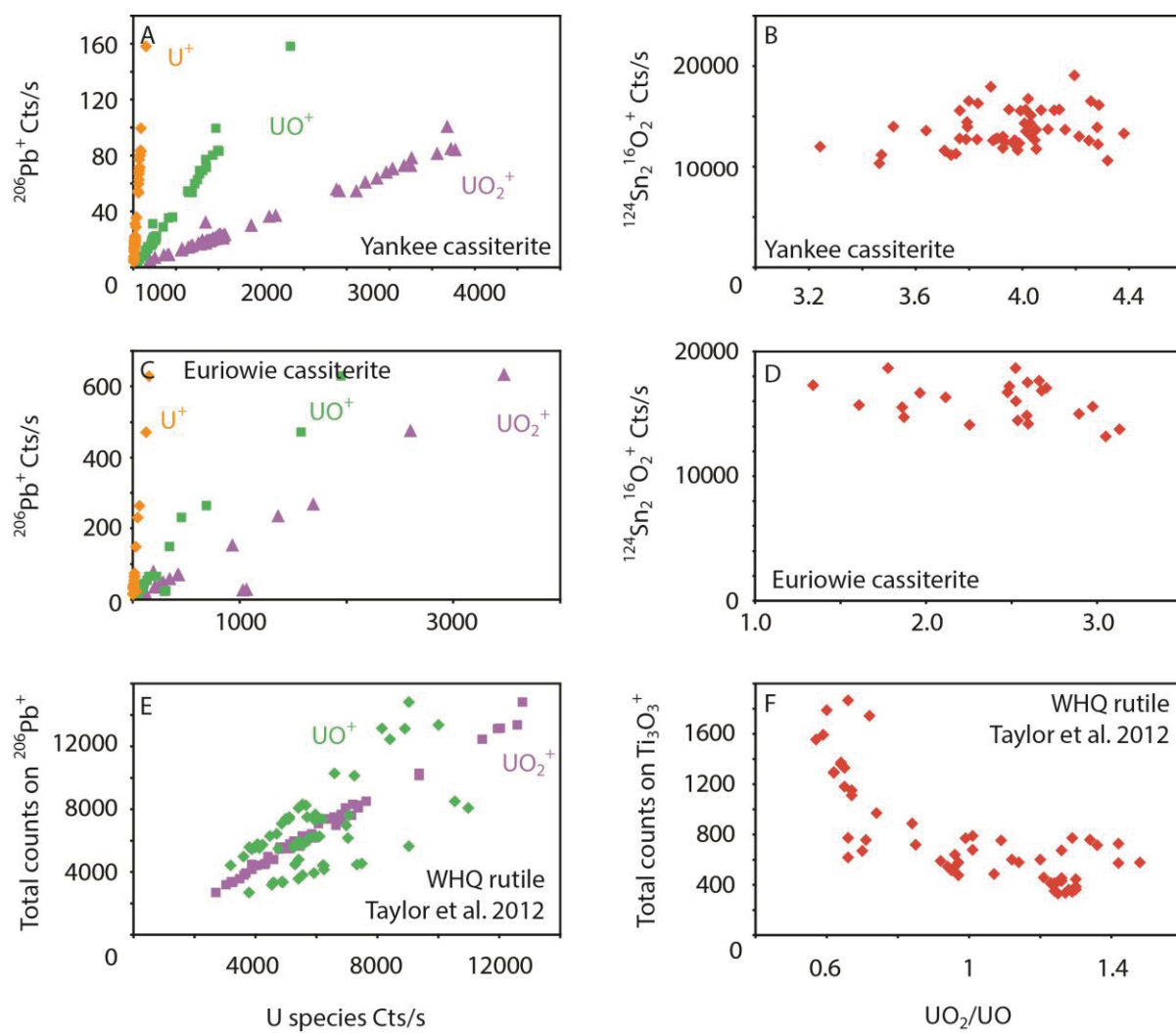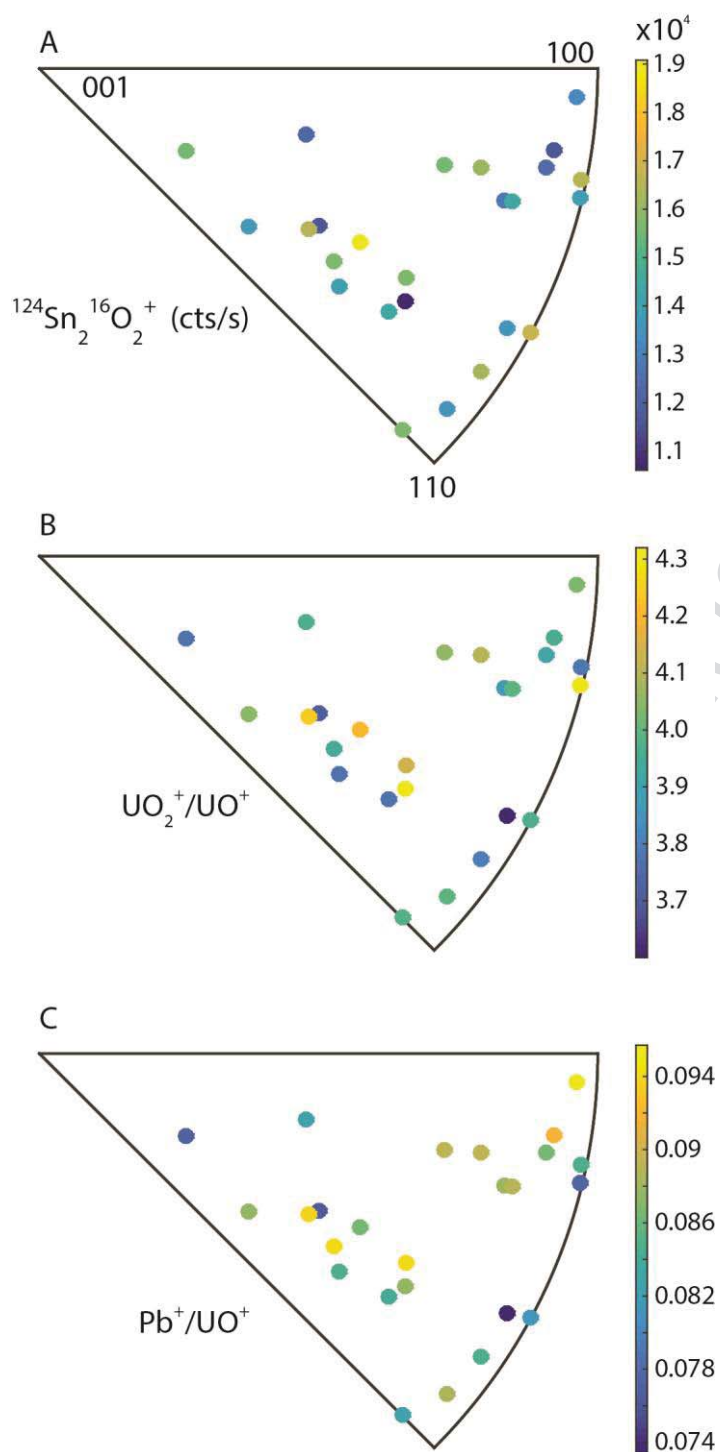
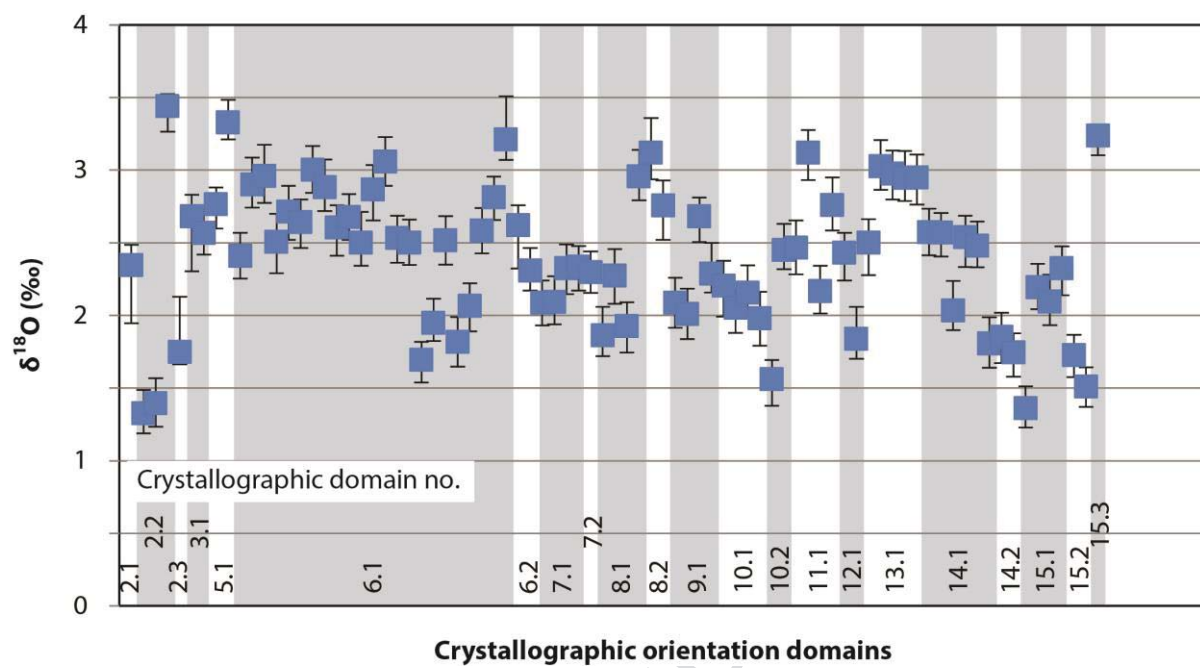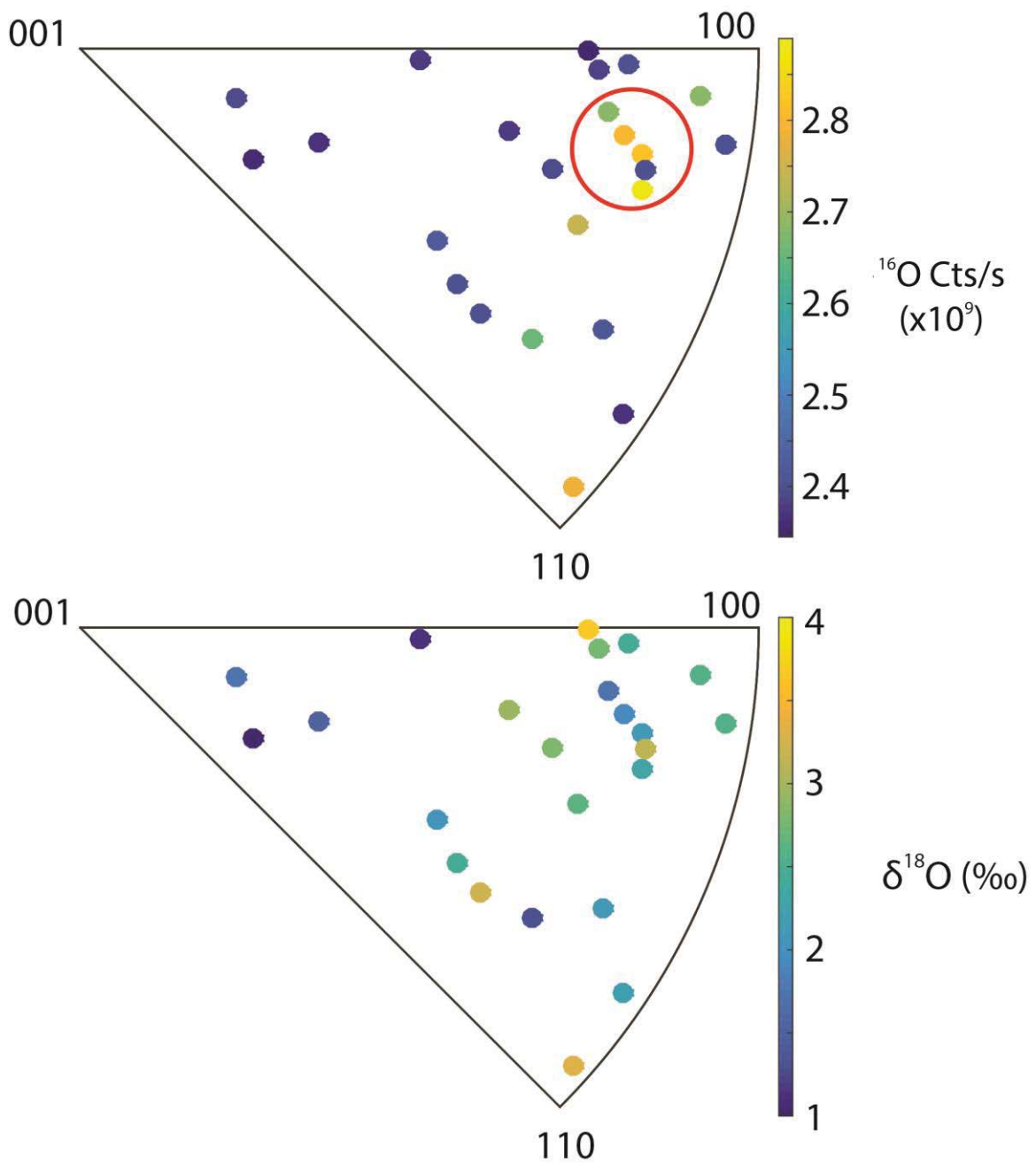**Figure 8**
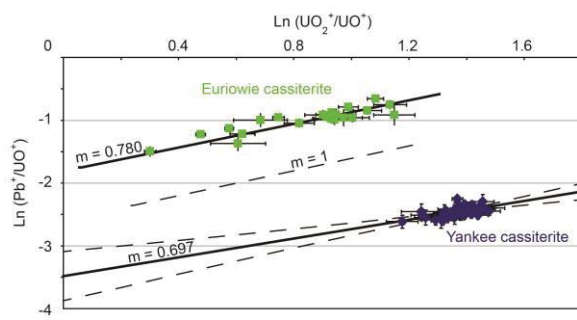
Figure 9
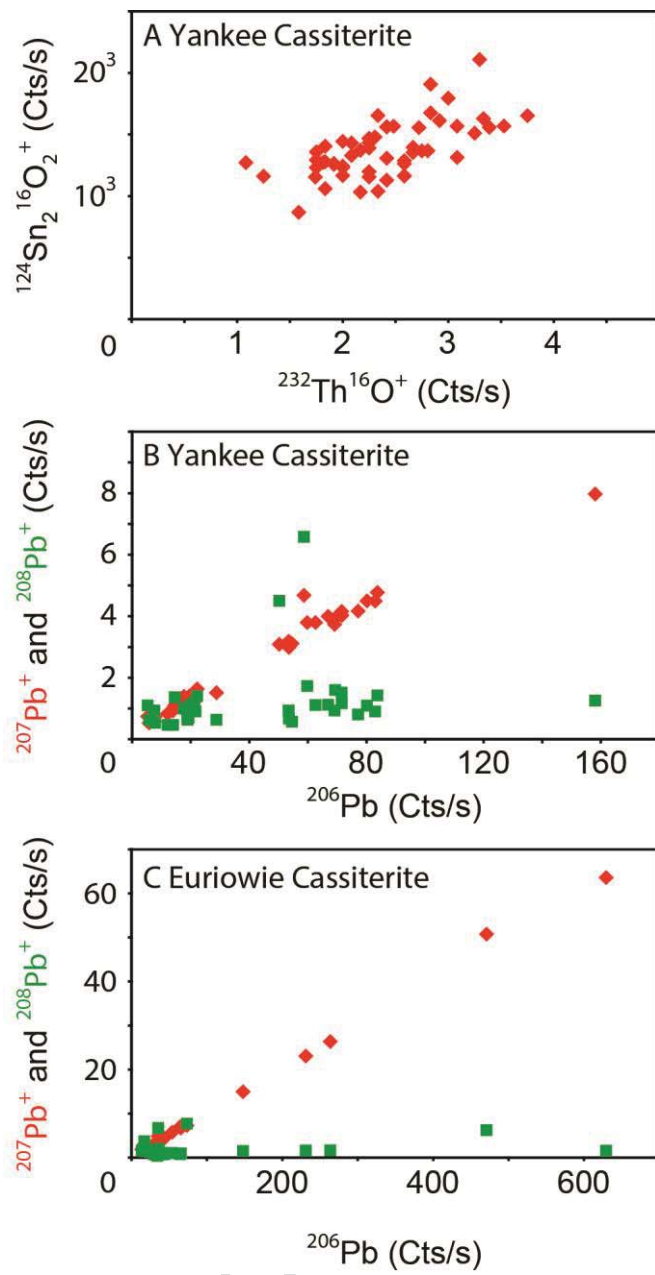
Figure 10

Figure 11

Figure 12

Table 1: Summary of SHRIMP 206Pb/238U age data for the Yankee cassiterite.

Weighted means were calculated for each crystallographic orientation.

Y1.2	2	258	21	259	21
Y1.3	4	244	24	244	24
Y3.1	4	242	13	243	13
Y4.1	2	242	35	242	33
Y5.1	2	241	36	247	32
Y5.2	1	256	13	243	33
Y6.1	2	240	31	244	24
Y6.2	1	255	15	254	15
Y6.3	2	242	28	242	28
Y7.1	2	251	24	253	24
Y7.2	2	232	24	231	24
Y8.1	2	230	26	233	27
Y8.2	2	246	18	246	18
Y9.1	2	229	24	260	13
Y10.1	1	260	13	260	13
Y10.2	1	244	29	249	29
Y10.3	1	262	16	265	16
Y11.1	1	223	12	223	12
Y11.2	1	249	15	250	15
Y13.1	1	233	14	234	14
Y14.1	1	244	33	248	33
Y15.1	1	227	13	226	13
Y15.2	1	249	13	251	13
Y16.1	1	252	13	253	13
Y17.1	2	244	20	245	20
Y18.1	1	230	12	227	12
Total		242.9	4.8	243.9	4.8

Table 2: SHRIMP 207Pb/206Pb age data for the Euriowie cassiterite.

Crystallographic domain	Uncorrected $^{207}Pb/^{206}Pb$ Age with 1σ uncertainty		208 corrected $^{207}Pb/^{206}Pb$ Age with 1σ uncertainty	
E1.1	2251	270	2128	228
E1.2	1692	125	1593	147
E2.1	1737	109	1648	123
E3.1	1687	46	1663	52
E4.1	1595	139	1509	174
E4.2	1423	158	1264	237
E4.3	1649	143	1475	183
E4.6	1645	160	1481	211
E5.1	1807	304	1202	484
E5.2	2375	289	1392	421
E5.3	2143	285	1470	370
E6.1	1633	122	1534	150
E6.2	1641	276	1107	454
E6.3	1798	24	1674	42
E6.4	1612	112	1538	138
E6.5	1644	35	1625	40
E8.1	1606	28	1547	37
E8.2	1529	48	1512	60
E8.3	1522	52	1457	68
E8.4	1610	53	1567	64
E9.2	1421	127	1306	185
E13.1	2049	185	1886	184
E13.2	1397	147	1337	211
Total	1666	51	1588	42

Table 3: SHRIMP SI δ18O average values for each crystallographic domain in the Elsemore Cassiterite.

Variations reflect isotopic heterogeneity rather than orientation effects.

Crystallographic domain	No. of analyses (rejected)	Average δ18O	2SD
E2.1	1	2.35	0.80
E2.2	3 (1)	1.36	0.10
E2.3	1	1.75	0.17
E3.1	2	2.62	0.16
E5.1	2	3.05	1.30
E6.1	23 (1)	2.58	0.79
E6.2	2	2.46	0.44
E7.1	4	2.21	0.28
E7.2	1	2.30	0.28
E8.1	4	2.25	1.00
E8.2	2	2.94	0.51
E9.1	4	2.27	0.60
E10.1	4	2.10	0.20
E10.2	2	2.00	1.25
E11.1	4	2.63	0.82
E12.1	2	2.13	0.84
E13.1	5	2.88	0.43
E14.1	6	2.33	0.66
E14.2	2	1.80	0.15
E15.1	4	1.99	0.86
E15.2	2	1.62	0.30
E15.3	1	3.24	0.27
Total		2.40	0.97